A Fully Cryogenic Phased Array Camera for Radio Astronomy

German Cortes-Medellin, *Member, IEEE*, Amit Vishwas, Stephen C. Parshley, Donald B. Campbell,
Phil Perilatt, Richard Black, *Student Member, IEEE*, Jay Brady, Karl F. Warnick, *Fellow, IEEE*,
and Brian D. Jeffs, *Senior Member, IEEE*

Abstract—We have developed a fully cryogenically cooled phased array feed (PAF) prototype camera and tested it on the Arecibo Radio Telescope in the summer of 2013. The camera consists of 19 dual-polarized elements on a hexagonal grid. The array elements are modified sleeve dipoles specially designed to be reinsertable, to include a noise injection coupling port and to operate at 18 K. Experimental results for observations on the Arecibo Telescope demonstrate performance of the cryogenic amplifiers, digital beamforming, and sensitivity over the PAF field of view, and provide an important proof of concept for a full-scale PAF receiver.

Index Terms—Cryogenics phased array camera, digital beamforming, radio astronomy.

I. INTRODUCTION

THE PURSUIT of phased array technologies, enabling instantaneous access to the field of view (FOV) of a telescope's optics, is one of the technology paths stated in the 2010 Astronomy Decadal Survey [1], which promises to attain gains in mapping speed of orders of magnitude in current and future radio telescopes. Work on phased array feed (PAF) systems for radio astronomy has been ongoing in Australia and the Netherlands, driven generally by the Square Kilometer Array (SKA) project and, specifically, by the desire to instrument ASKAP, the 36 antenna Australian SKA Pathfinder [2], and the Dutch Westerbork array [3] with PAFs. In the USA, PAF development for radio astronomy has been pursued by collaborations between the National Radio Astronomy Observatory (NRAO) and Brigham Young University [4] and by Cornell University [5].

Unlike scanned phased arrays, these cameras fully sample the incoming electromagnetic radiation in the FOV of the telescope focal plane and digitally synthesize multiple beams simultaneously. In practice, the beams (pixels) can be spaced much more closely on the sky than the ones resulting from multiple horn systems, allowing the telescope's FOV to be completely sampled. PAF's can also adapt to a particular telescope's optics, correcting for aberrations and maximizing signal to noise (S/N) over the available FOV. These advances are being achieved at the expense of considerable complexity in digitally forming the beams, which requires processing at very high data rates. Typically, 60–90 dual-polarization elements need to be sampled at bandwidths of hundreds of mega hertz. However, the tremendous advances in digital processing speed have made digital beamforming over 300–500 MHz bandwidths quite feasible [6].

The ASKAP PAF has 188 (not aligned polarized) elements and will synthesize up to 36 beams with a bandwidth of 300 MHz. The Apertif PAFs on the 14-antenna Westerbork array will have 121 elements (60 in one polarization, not aligned with 61 in the other polarization), and synthesize 37 beams on the sky. Because of the large number of antennas to be equipped with PAFs, both the ASKAP and the Westerbork PAF systems operate at room temperature and had the goal of achieving total system temperatures (Tsys) of less than 55 K. The estimate for the Apertif system is now 70 K due to provision for RFI mitigation.

An important figure of merit (FoM) for PAF systems for radioastronomy applications is the *survey speed* [7], [8]. Let N_Q be the number of instantaneous *nonoverlapping formed beams* by the array, then the survey speed is proportional to

$$SVS \propto N_Q \Omega_H BW (A_{\text{eff}}/T_{\text{sys}})^2 \qquad (1)$$

where Ω_H is the half power beam *solid angle*, BW is the system bandwidth (assuming continuum observation), A_{eff} is the effective aperture of the telescope, and T_{sys} is the system temperature.

Therefore, maximizing mapping speed is accomplished by increasing the number of nonoverlapping instantaneous beams on the sky, and/or increasing the bandwidth, and/or increasing the overall system sensitivity, i.e., either by increasing the effective aperture or decreasing the system temperature. For a given A_{eff}, a reduction in system temperature will increase the survey speed quadratically, hence the interest in cryogenic
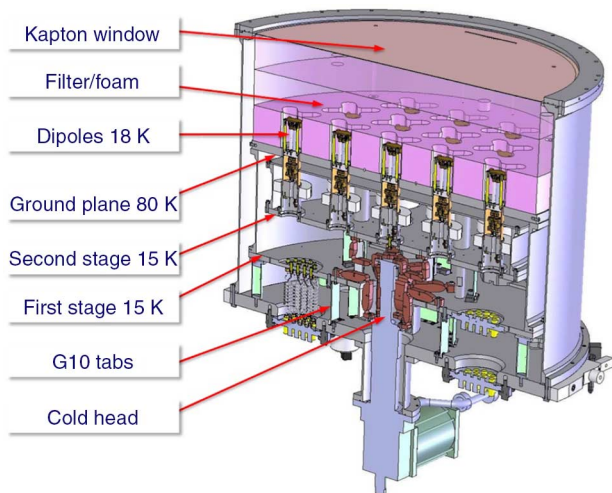
Fig. 1. Cross-sectional view of the AO19 cryo-PAF camera.

PAF systems. Likewise, the quadratic aperture term favors large aperture radio telescopes, such as the Arecibo 305-m radio telescope [9], and the 100-m Green Bank Telescope [10], as suitable platforms to be equipped with a cryogenic PAF system, with the goal of achieving system temperatures close to what is now current with single and multiple feed horn technology.

In 2011, we completed a PAF feasibility study [5], which determined that the 1-dB available FOV of the Gregorian optics of the Arecibo telescope is an ellipsoid of $16 \, \text{arcmin} \times 20 \, \text{arcmin}$ in size. A full-sized PAF camera will require about 85–91 elements on a hexagonal grid of approximately 115 cm in diameter [9]. Therefore, one of the first challenges that we faced to build a cryogenic PAF camera was the large vacuum window.

We have developed a 19-element, dual-polarized, fully cryogenic PAF prototype camera for the Arecibo radio telescope (AO19 cryo-PAF), which demonstrated two key milestones for the development of cryogenic PAF systems, namely the feasibility of a 70-cm diameter vacuum window that is transparent at radio frequencies, and a system temperature of 35 K. This camera was deployed at the Arecibo radio telescope in Puerto Rico for system testing during the months of July and August 2013. We present here details of the development of this prototype camera and results of the measurements.

II. SYSTEM DESCRIPTION

The AO19 cryo-PAF camera consists of 19 dual-polarized dipole elements enclosed inside of a cylindrical cryostat. Fig. 1 shows a cross-sectional view of the main components of the camera. The vacuum window has a diameter of 70 cm and consists of a Kapton film supported by a radio-transparent foam.

A. Cryogenic Design

The cryostat is cooled by a dual-stage CTI 1050 Cryodyne cryocooler. The CTI 1050 is capable of providing 3 W of lifting heat power at 15 K and 60 W at 70 K simultaneously. The 70-K cold head is attached to the bottom plate of the first stage, and
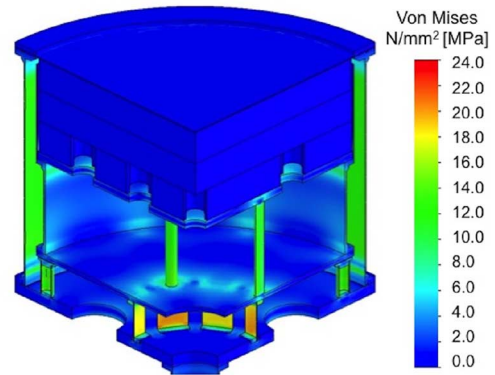

Fig. 2. Static stress model verification of the cryostat foam and first stage design supporting the vacuum load.

the 15-K cold head to the bottom plate of the second stage, by flexible copper links.

The final operating temperature of the ground plane is 80 K, while the dipole/LNA packages, which are attached to the bottom plate of the second stage, were operating close to 15 K (LNAs) and 18 K (dipoles), respectively.

A tradeoff between thermal and structural loads was made in the design to support approximately 4 metric tons of atmospheric pressure on the 70-cm-diameter vacuum window. This was accomplished by transferring the atmospheric load to the ground plane (top plate of the first stage) through a closed-cell foam called ROHACELL [11] capable of supporting compression loads in excess of 1.5 MPa.

The ground plane is supported by the first-stage external shield and a ring of six columns, which transfer the atmospheric load from the front to the first-stage back plate. From there, an inner ring of G10 flexures and an outer ring of G10 columns transfer the load to the bottom plate of the cryostat, which is then balanced by atmospheric pressure. The G10 flexures are also used to structurally support and thermally isolate the second stage (15 K) from the first stage (70 K). Fig. 2 shows a plot of the von Mises stress across the assembly due to an 1-atm vacuum load (0.1 MPa) from our FEA static vacuum load modeling. We use it to compare to individual materials' yield stresses to access the robustness of our design. We found all materials to be below their yield stresses; in particular, a maximum of 0.32 MPa was obtained for the foam (in the lower layer).

We used three layers of the ROHACELL foam, 7.5 cm thick each, in order to reduce the thermal load on the first stage to a reasonable level, see Fig. 3. The layers have small foam tabs that serve as an interlocking mechanism to suppress any lateral displacements. The lower layer includes dipole-shaped carvings to avoid any contact with the 18-K dipoles as shown in Fig. 4. Also this figure shows the foam thermal shield, attached to the 80-K ground plate, surrounding the walls of the foam (not in direct contact with the foam). This shield is necessary to reduce the thermal loading on the first stage because although the foam is a poor thermal conductor, it has a very high emissivity and when exposed to room temperature radiation, it can transfer significant heat (approximately 10 W).

Since the foam is in direct contact with the 80-K plate, a careful thermal analysis was performed to assess the total thermal
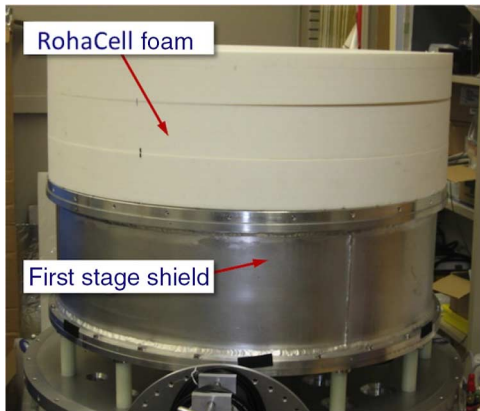
Fig. 3. Detail of the three layers of ROHACELL foam on the top plate of the first stage.
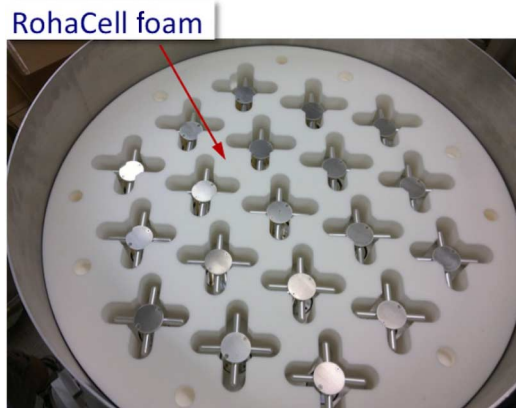

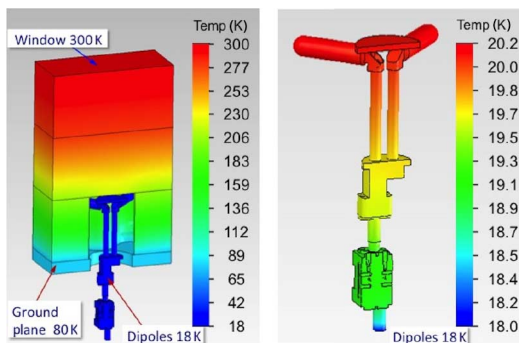Fig. 4. Detail of the dipole shaped cutouts in the first layer of foam.

Fig. 5. *Left*: temperature distribution based on the thermal modeling of the foam and dipole cell. *Right*: expected final dipole temperature distribution when the base of the LNA is maintained at 18 K.

load. Fig. 5 shows the calculated temperature distribution of a typical single-dipole cell of foam, including the dipole and LNA with an expected 20 mW of thermal load from each LNA in the dipole package. The results indicated that if a temperature of 18 K is maintained at the LNA base plate, the final dipole top plate temperature is 20 K during operation. In our experiment, we found that the measured LNA temperatures varied from 14 to 15 K (17 to 18 K for the dipoles) from the center to the periphery of the ground plate, respectively, lower than our design calculations.
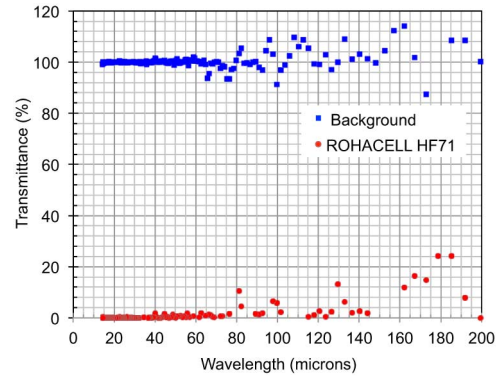

Fig. 6. Measured IR transmission of the ROHACELL HF 71 foam with an FTS.

Fig. 7. Kapton vacuum window.

We corroborated that the foam is an excellent IR filter by measuring its transmission characteristics with a Fourier transform spectrometer (FTS), between 10 and 200 µm, see Fig. 6. The measurement shows that the foam is mostly opaque in this wavelength range and is an excellent absorber of room temperature thermal radiation.

Although the foam has excellent mechanical and thermal properties, it can not maintain a high vacuum. We use a kapton film as a final vacuum barrier. Fig. 7 shows a view of the Kapton vacuum window.

The Kapton film is 125 µm thick and is bonded to the back of the window flange. The vacuum O-ring sits between the Kapton film and the vacuum vessel flange.

Fig. 8 shows results from the first cool down for pressure and temperature versus time (in 24-h labels) for the full cryostat assembly. Note that the pump-down time improved with subsequent cycles. At around 10^{-3} mbar, the cryocooler was started. The final pressure was 5×10^{-7} mbar and the temperatures were approximately 65 K for the first stage, and 12 K for the second-stage base plates, respectively. These tests indicated not only that the large vacuum window design works very well but also that it is easily scalable to the large final instrument camera with a diameter of about 120 cm.

B. Electromagnetic Design

The AO19 cryo-PAF elements are specially designed, dual-polarized sleeve dipoles [12], with an operating bandwidth from 1.2 to 1.7 GHz. The dipole design incorporates a balun with
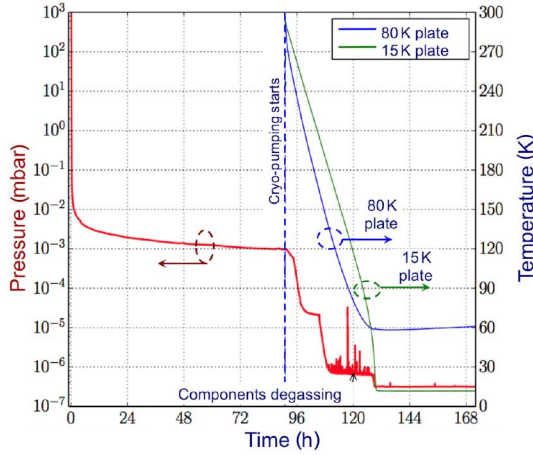
Fig. 8. Measured cryostat pressure and temperature cool-down curves for the first cool down.

Fig. 9. Dipole array over the ground plane. Arrow highlights thermal gap between dipoles and ground plane.
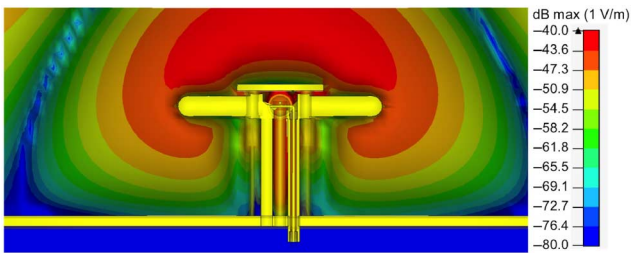

Fig. 10. Electromagnetic modeling of the modified sleeve dipole and balun: electric field on the plane of symmetry at 1.4 GHz.

a 50-Ω input coaxial line for each polarization port, and a balanced common noise injection port, for noise calibration. Fig. 9 shows a closeup of the dipole array that includes the thermal gap between the ground plane and the dipole base. This gap dimension was designed to have the first resonance above 2.8 GHz.

The dipole design with balun was developed using CST Microwave Studio [13] with the design optimized to provide a very wide frequency response between 1.2 and 1.7 GHz. Fig. 10 shows the calculated E-field, on the plane of symmetry.

Fig. 11 shows a comparison between the calculated and measured input match on each polarization port as well as the noise coupling (port 3) to both ports for dipole #6 (label shown in Fig. 12). The input match is better than -10 dB from 1.15 to
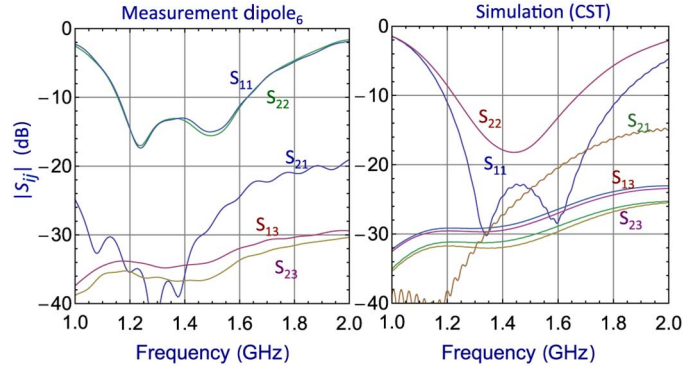

Fig. 11. Simulated versus measured S-parameters, Pol-A (VERT), Pol-B (HORZ), and noise coupler ports.
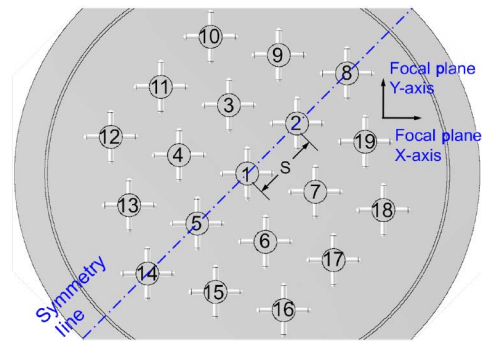

Fig. 12. Front view detail of the AO19 cryo-PAF model indicating the dipole separation, nomenclature, symmetry line, and orientation of the dipole arms with respect x- and y-axes.

1.65 GHz. The noise coupling target design was -30 dB with balanced coupling to both polarizations, but the realized coupling is close to -35 dB between the two polarizations. The input match and noise coupling have small variations across the dipoles in the array.

The array elements are arranged on a hexagonal grid pattern with a separation $s = 128$ mm (see Fig. 12). The dipoles' arms are rotated $45°$ with respect to the hexagonal grid in order to balance and minimize coupling between the elements.

The analysis of the full array, including the cryogenic ground shield, was also done using CST Microwave Studio. In order to reduce the memory requirements during the simulation, the complete cryostat model is rotated $45°$ counterclockwise to align the dipole arms with the x- and y-axes, as indicated by the symmetry line in Fig. 12.

Fig. 13 corresponds to a snapshot of the calculated electric three-dimensional (3-D) field response of the array at a particular E-field phase value when the vertical port of dipole #2 is excited. It is possible to appreciate the influence of the other dipoles in the array on the field, in particular, the degree of coupling depending on the distance from dipole #2. In the two-dimensional (2-D) field projection on the right centered on dipole #2, we can see the spherical wave emanating from the dipole and its distortion due to the presence of the other dipoles and the walls of the cryostat.

For the purpose of a qualitative comparison, Fig. 14(*left*) shows the calculated 3-D radiation pattern response of a
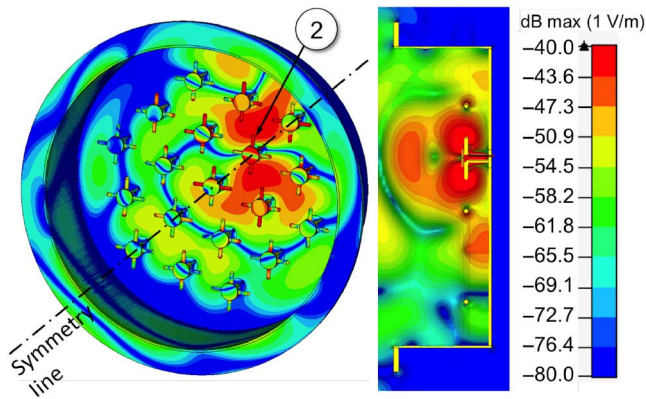
Fig. 13. Electromagnetic modeling of the entire dipole array in the cryostat. *Left:* the electric field when dipole #2 is excited, at 1.4 GHz. *Right:* an E-field cut for dipole #2.
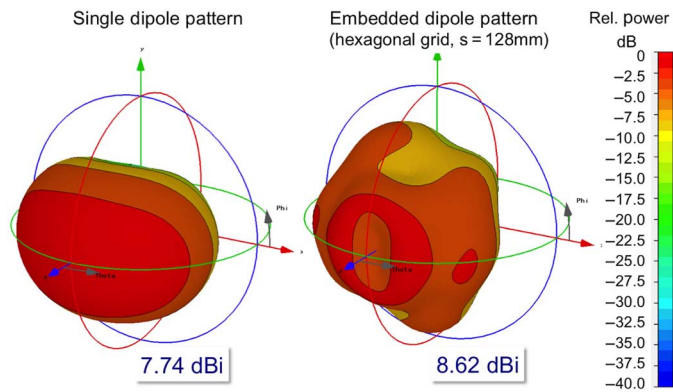

Fig. 14. *Left*: calculated radiation patterns (vertical polarization) for a single dipole element. *Right*: embedded center dipole in the array (128 mm spacing).

Fig. 15. Calculated normalized radiation patterns cuts (for $\phi = 0°, 45°$, and $90°$) for the single-dipole element over a finite ground plane, at 1.4 GHz and vertical polarization.

Fig. 16. Calculated normalized radiation patterns cuts (for $\phi = 0°, 45°$, and $90°$) for the the embedded dipole element in a hexagonal grid (128 mm spacing), at 1.4 GHz and vertical polarization.

single-dipole element over a ground plane, and on the right, the embedded radiation pattern for the center dipole inside the cryostat. The single element has a peak directivity of 7.7 dB over isotropic, whereas the embedded response inside the thermal shield of the cryostat is 0.9 dB more directive, at 8.6 dBi, but with a lower value in the middle.

Fig. 15 shows normalized radiation pattern cuts as a function of θ with $-180° \leq \theta \leq 180°$, and with ϕ-cuts at $\phi = 0°, 45°$, and $90°$ for the single dipole over a ground plane, at 1.4 GHz and vertical polarization. The cross-polarization component is indicated in the figure along with the respective ϕ-cuts.

Fig. 16 shows similar normalized radiation pattern cuts as a function of θ for the embedded dipole in the hexagonal (128-mm spacing) grid inside the cryostat, at 1.4 GHz and also vertical polarization. The pattern cuts indicate more clearly the reduction in the axis gain of the embedded dipole response, with a peak directivity now on a ring between 10° and 20° from boresight. Although there is an increase in the embedded element cross-polarization, through the shaped optics of the Arecibo telescope, the element produces a beam in the sky with a peak cros-pol better than -20 dB.

Fig. 17 shows the calculated embedded radiation patterns for all dipoles at 1.4 GHz aligned with the corresponding element position, for vertical polarization (Pol-A). We found that while the cryostat wall increases the directivity of the element patterns
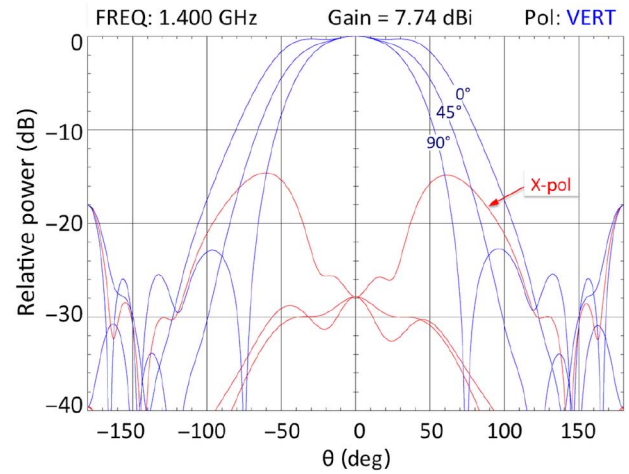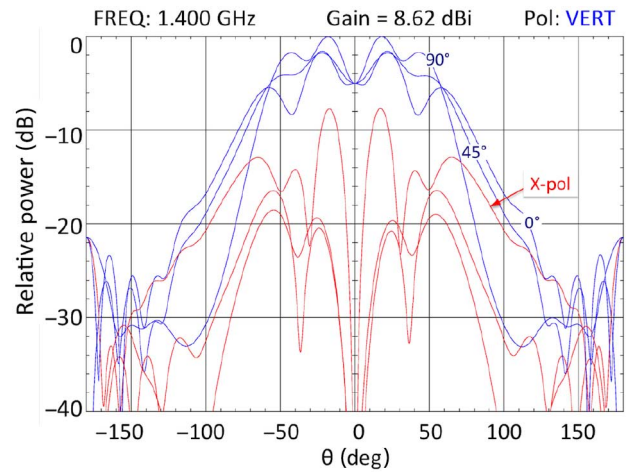
by about 2 dB, it also, as expected, distorts the element patterns. Nevertheless, the sky beams through the optics are still well defined (see Fig. 26).

The particular ROHACELL foam that we chose for the cryo-camera is ROHACELL 71 HF, which has special high-frequency characteristics, with an extremely low dielectric constant ($\sim$1.075 and loss tangent of $\tan \delta < 0.0002$ at 2.5 GHz). In the simulation, we assessed the effect of this material on the dipoles' radiation patterns and input match, but there was no noticeable effect on either.

We have developed a very comprehensive electromagnetic model of the Arecibo telescope's optics, including the shaped reflectors of the Gregorian corrector system [5]. This allows us to calculate the complete far-field pattern of any feed at the focal plane of the telescope, as shown in Fig. 18. The far field is obtained by aperture integration methods of the fields on the aperture plane of the telescope. We used the embedded dipole patterns calculated previously by the CST Microwave studio simulations and convert them into an spherical wave expansion
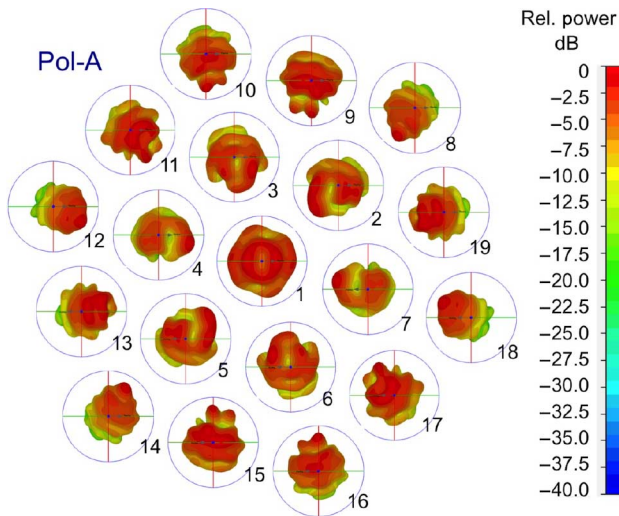
Fig. 17. Mosaic of the calculated embedded radiation patterns for all the dipole elements at 1.4 GHz localized at the corresponding element position for clarity. Pol-A.
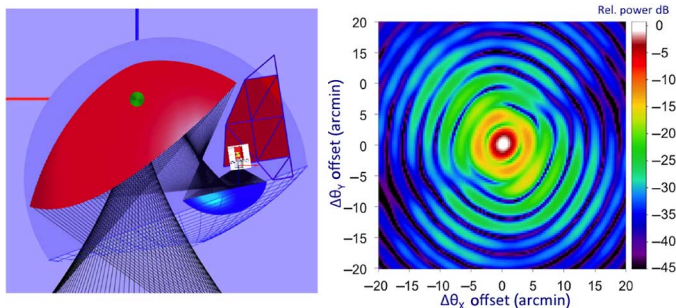

Fig. 18. Far field calculation through Arecibo optics. *Left*: detail of the secondary and tertiary reflector optics, with the AO19 cryo-PAF at the focus. *Right*: calculated normalized far field radiation pattern on the sky produced by dipole 1, Pol-B at 1.4 GHz.

form to be used as an input to our Arecibo modeling optics program. Fig. 18 (*right*) shows the calculated far-field pattern produced by the central dipole (Pol-B) element in the array at 1.4 GHz. In the figure, the HPBW is 4.1 arcmin with a peak side lobe level of -12.7 dB.

C. Cryogenic LNA Package

A special dual-polarization sleeve dipole/LNAs package was developed (see Fig. 19) to thermally connect it to the 18-K cryogenic plate. It has also custom-made press-fit RF connectors for easy insertion and extraction, which allows servicing through the front opening of the cryostat in a plug-and-play style manner. The press-fit connectors provide dc bias, lines for voltage and current monitoring, and three RF ports for Pol-A, Pol-B, and noise injection (Fig. 20).

Our current LNA design, based on [14], consists of a two-stage amplifier that uses a commercial packaged SiGe transistor (NXP BFU 725) along with SMT (surface-mounted technology) components bonded on a very low loss Teflon substrate PCB. There are two boards integrated back-to-back in the carrier.
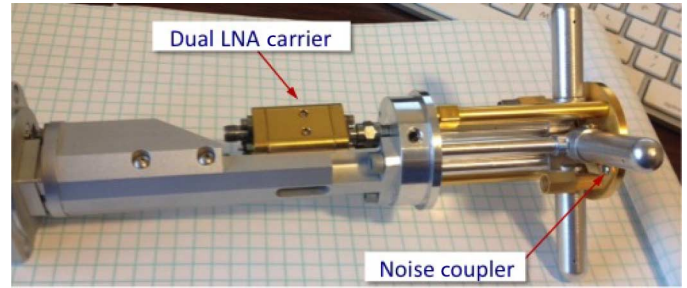
Fig. 19. Dipole with cryo-LNA package.

Fig. 20. LNA carriers open side: Pol-A, opposite side: Pol-B. Connectors provide DC bias, lines for voltage monitoring, and 3 RF ports for Pol-A, Pol-B. and noise injection.
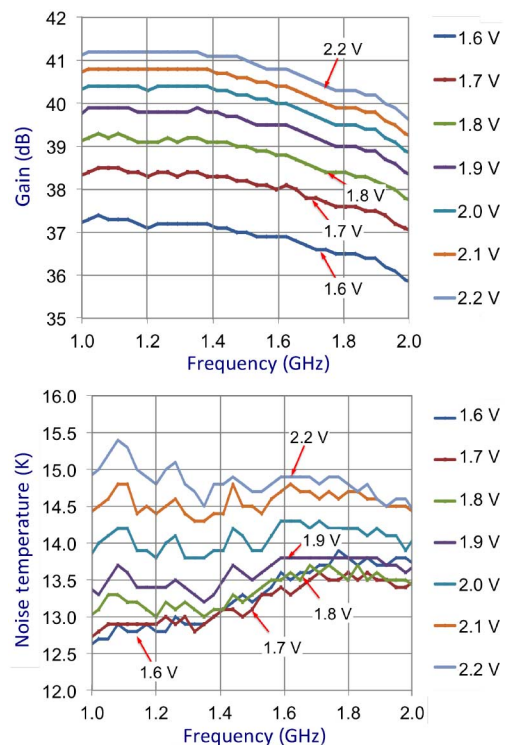
Fig. 21. Measured gain (*top*) and noise temperature (*bottom*) of a typical cryo-LNA as a function of frequency for different bias voltages, at 15 K.

Fig. 21 shows typical gain and noise temperature measurements for these LNA carriers at a physical temperature of 15 K, as a function of frequency, and for various bias voltages. At this temperature, the manufactured LNAs have a typical gain of 39 dB and noise temperatures of 14 K.
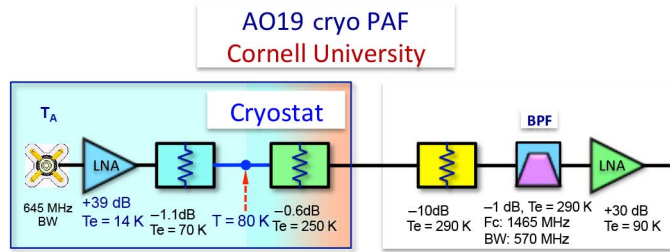
Fig. 22. System architecture of the AO19 cryo-PAF camera.

D. System Architecture

Each system channel in the AO19 cryo-PAF camera system consists of a dual-polarization dipole antenna element, a cryogenic LNA at 15 K, followed by two sets of stainless steel coax cables (from 18 to 70 K, and from 70 K to room temperature), which reduce the thermal loading between stages. The first set is 70 cm in length each (3×38 cables), located between the 18-K stage and the 70-K stage. The second, 40 cm long, connects the 70-K stage and the 300-K back plate of the cryostat. Feedthrough is provided by two 20-port hermetic SMA connectors, which collect all the Pol-A and Pol-B channels together.

Outside the cryostat we have a -10 dB attenuator, followed by a band pass filter, centered at 1.465 GHz, with an effective bandwidth of 570 MHz. This band pass filter serves to avoid saturation of a second, room temperature amplifier by off-band spurious signals. The system architecture is shown in Fig. 22. Using the embedded dipole pattern, we estimated an antenna temperature of the order of 35 K, at the flange of the dipoles (looking toward the tertiary mirror inside the Arecibo Gregorian dome); assuming a noise temperature of 14 K for the LNA, the calculated single element system temperature on the sky is approximately 52 K.

For monitoring and control (M&C), we used a National Instruments controller [15] NI PXIe-1071 with interfaces to read the temperature sensors, vacuum sensor, and the current bias of each amplifier. For measuring the currents, we use a custom fan-out board, connected to the NI controller. All external components were enclosed inside an RF-shielded enclosure for operation on the Arecibo Telescope's Gregorian rotary floor, with only fiber-optic ethernet connection and RF coax connections, for signal transport and calibration noise injection.

III. Testing at the Arecibo Observatory

We deployed the prototype at the Arecibo Observatory in late July 2013 (see Fig. 23), and testing was conducted in conjunction with the Brigham Young University PAF group led by Karl Warnick and Brian Jeffs, and Arecibo Observatory personnel. The BYU group provided the down converters, digitizing system, and several levels of beamforming capability.

After a postshipment check, it took 2 days to evacuate and cool down the cryo-PAF until it reached nominal operating conditions of vacuum and cryogenic temperatures. An initial interface with the BYU back-end system was done on the ground by making ON/OFF Y-factor measurements using the sky and a room temperature absorber, as the cold and hot
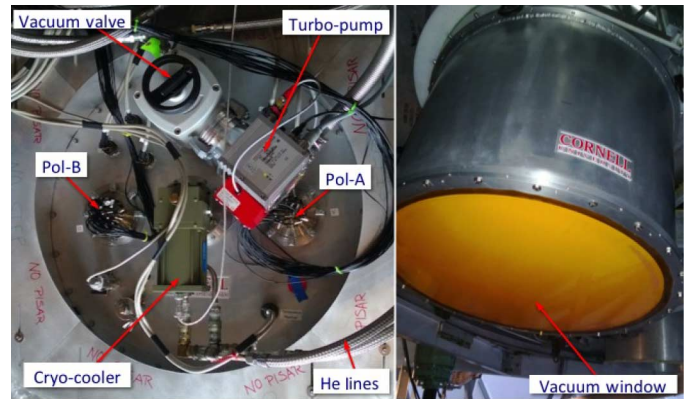

Fig. 23. AO19 cryo-PAF mounted in the AO's Gregorian rotary floor. *Left:* view from above the floor. *Right:* view from below.
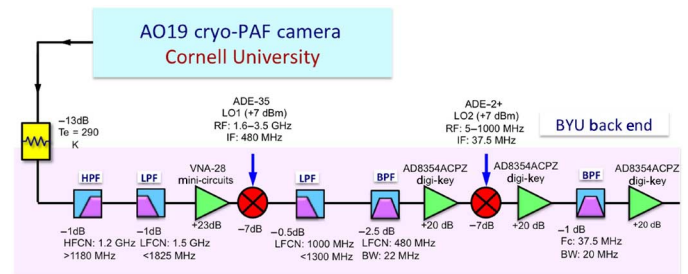

Fig. 24. Back-end receiver downconverter card system used in each system channel in the array.

loads. A small metallic conical skirt was used around the vacuum window to minimize ground-related noise temperature coupling.

A. Digital Beamforming System

The BYU back-end system used in the Arecibo experiment is comprised of two subsystems: an analog receiver/downconverter, followed by a digital receiver/beamformer. The analog receiver/downconverter includes 16 RF cards; each with four receiver chains, allowing for up to 64-L-band input signals. For the AO19 experiment, 38 ports were used, one for each PAF array element and polarization.

Each analog receiver has two mixing stages; the first IF frequency is 480 MHz and the final IF output bandwidth of 20 MHz is centered at 37.5 MHz as shown in Fig. 24. This places the passband in the second Nyquist zone for base-band bandpass sampling at 50 Msamp/sec by the following analog-to-digital converter (ADC) stage. The 20-MHz passband may be tuned anywhere in the range of 1.2–1.8 GHz by computer control of the first mixer local oscillator.

This 64 input synchronously sampled ADC is part of the digital receiver/beamformer which is implemented on a CASPER ROACH FPGA system [16] using custom firmware. This is shown schematically in Fig. 25. In addition to digitizing the PAF array signal, the digital receiver performs the following functions:

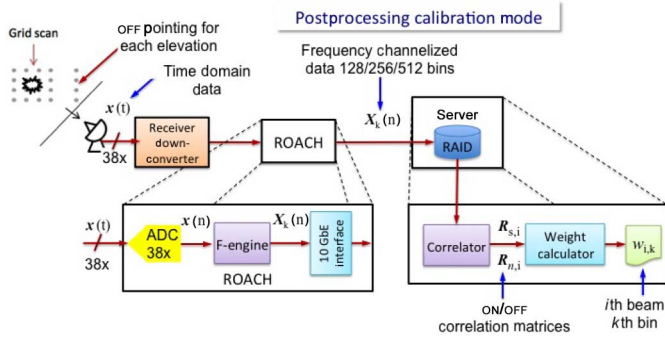1) Frequency channelization with a polyphase filter bank/FFT F-engine for all 64 inputs. Channel bandwidth is 98 kHz.

Fig. 25. Postprocessing digital beamforming used in the experiment.

2) Digital mix down to complex base-band for each frequency channel.
3) Continuous streaming to a disk RAID array for postprocessing of a user-selected subset of frequency channels. With the 38 inputs for the AO19 cryo-PAF, up to 92 channels of base-band complex data (9-MHz total bandwidth) can be continuously recorded. This operational mode is critical for capturing raw unreduced data for future analysis to apply a variety of different correlator and beamforming algorithms after the data collection experiment. Postcorrelation beamforming is also supported by this mode.

B. Calibration

During postprocessing, we obtained the ON/OFF source correlation matrices, i.e., $\mathbf{R}_s$ and $\mathbf{R}_n$, respectively. Then, we computed the corresponding beam weights $\mathbf{w}$ that maximize signal-to-noise ratio (SNR), as shown in (2) and (3), and explained in detail in [17]

$$\text{SNR} = \frac{\mathbf{w}^H \mathbf{R_s} \mathbf{w}}{\mathbf{w}^H \mathbf{R_n} \mathbf{w}} \quad (2)$$

$$\mathbf{w}(\omega_s) = \mathbf{R_n}^{-1} \mathbf{a}_{\Omega_s} \quad (3)$$

where $\mathbf{a}_{\Omega_s}$ is the calibration vector in a particular $\mathbf{\Omega}_s$ direction. $R_s = \sigma_\nu^2 \mathbf{a}_{\Omega_s} \mathbf{a}_{\Omega_s}^H$ is the desired signal covariance matrix for a source with flux σ_ν arriving on the mainlobe peak for a beam steered to $\mathbf{\Omega}_s$, and $\mathbf{R_n}$ is the noise covariance matrix estimated by the off-source calibration pointing step described next.

For the cryo-PAF calibration, we chose several bright point radio sources with a typical flux density between 7 and 10 Jy to have good SNR. We formed a calibration grid centered at the point source with a spacing and overall grid size determined by the FOV of the array camera in the sky. We pointed the telescope to the calibration grid and took data in the direction of each grid pointing and also to off-source noise calibration locations.

Covariance matrices were processed for all grid points to estimate the steering vectors $\mathbf{a}_{\Omega_s}$ for each beam. For this experiment, we use one off-grid noise reference at the beginning and one at the end of the calibration run to estimate $\mathbf{R_n}$.
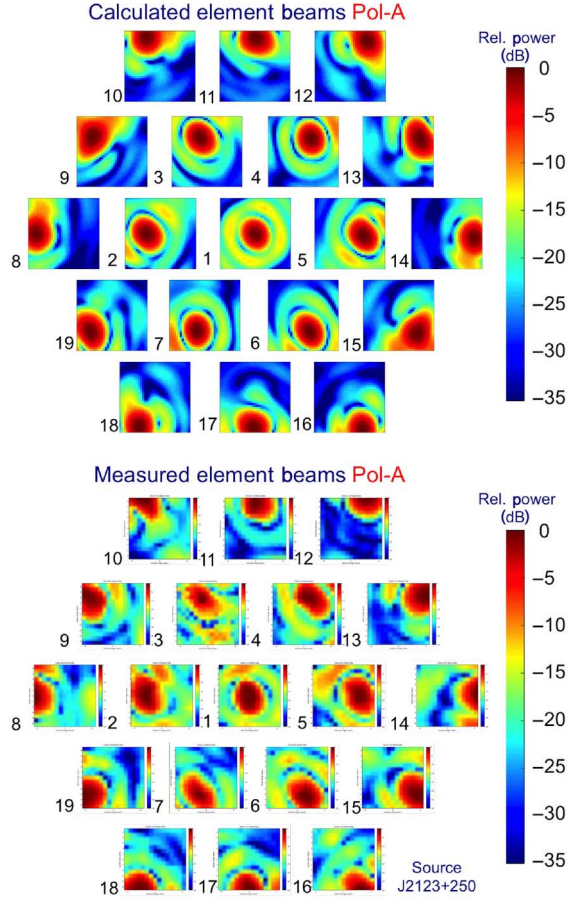

Fig. 26. Mosaic of telescope's normalized far field patterns in the sky produced by the cryo-PAF individual dipoles (Pol-A at 1.4 GHz). *Top:* calculated far field patterns. *Bottom:* measured far field patterns during calibration. Each square is 11 arcmin × 11 arcmin in size.

IV. RESULTS

Tests on the telescope took place between July 26 and August 4. The cryo-mechanical design worked very well, maintaining vacuum and nominal 15 K at the LNAs, and 80 K at the ground plane for the duration of the experiment. A few technical issues were encountered. Four LNAs failed, the reason appears to be due to the plastic packaging used in these commercial SiGe transistors that suffer from thermal stresses during the cryostat thermal cycling. However, we were able to obtain both sensitivity and formed beam data.

Figs. 26 and 27 show two set of mosaics of 19 beams in the sky. The *top* panels are the calculated individual dipole far-field patterns in the sky for Pol-A and Pol-B, respectively. On the *bottom* panels, we show the normalized system pattern response of the array, obtained normally as a byproduct of the cryo-PAF calibration, in this case, with a 10.35-Jy source (J2123 + 250), on a 15 × 15 calibration grid. Each individual subfield in the mosaic is approximately 11 arcmin × 11 arcmin in size, centered at the middle of the FOV, with the patterns normalized (scale in dB).

In general, there is good agreement in the location, shape, and orientation of the elliptical beam in the FoV, between the calculated and measured beams. First, side lobe levels are more
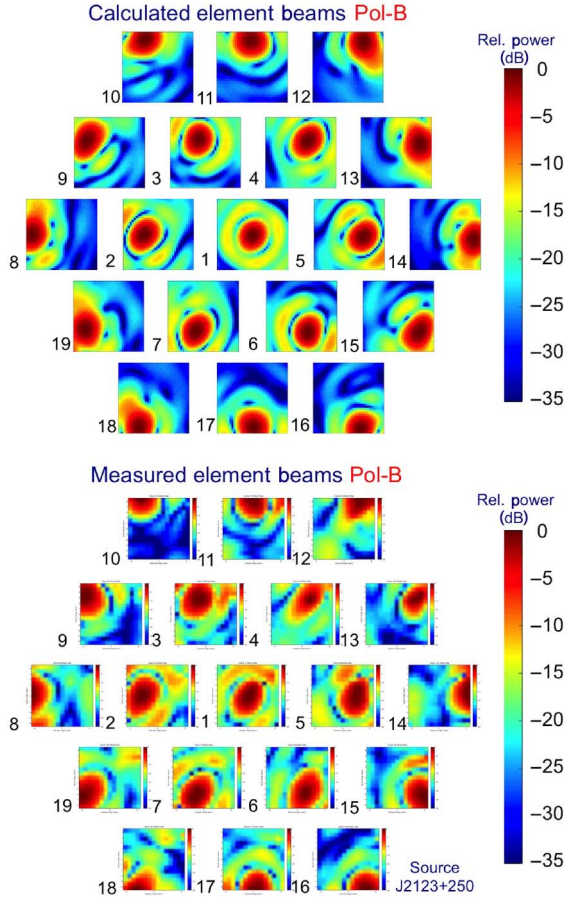
Fig. 27. Mosaic of telescope's normalized far field patterns in the sky produced by the cryo-PAF individual dipoles (Pol-B at 1.4 GHz). *Top:* calculated far field patterns. *Bottom:* measured far-field patterns during calibration. Each square is 11 arcmin × 11 arcmin in size.

difficult to compare. Although reasonably consistent with the calculated ones, they show more distortion.

Even though there are a few nonworking channels (i.e., 3-A, 4-B, 7-A, and 13-B), the array calibration process nonetheless produces a beam in those directions, albeit with diminished sensitivity (see further discussion following Fig. 29).

Fig. 28 shows the digitally formed beam patterns using Maximum SNR response, for Pol-A, at 1.3999 GHz, scanned by modifying the weights of the digital beamformer across the calibrated FoV. Notice that the synthesized beams are now more well defined and more circular in shape than the individual dipole measured beam responses. Although pure max SNR beamforming does not have side lobe control, the figure shows in most cases lower side lobe levels than the individual element responses.

One important FoM parameter for PAFs is the sensitivity defined by

$$\frac{A_e}{T_{\text{sys}}} = \frac{k_B BW}{\sigma_\nu} \frac{\mathbf{w^H R_s w}}{\mathbf{w^H R_n w}} \left[\frac{m^2}{K}\right] \tag{4}$$

where k_B is the Boltzmann constant, σ_ν is the source flux, and with maximum SNR weights $\mathbf{w}$ (3). Fig. 29 shows the combined (Pol-A+Pol-B) sensitivity plot in units of m^2/K obtained across the calibration field on the July 26 run.
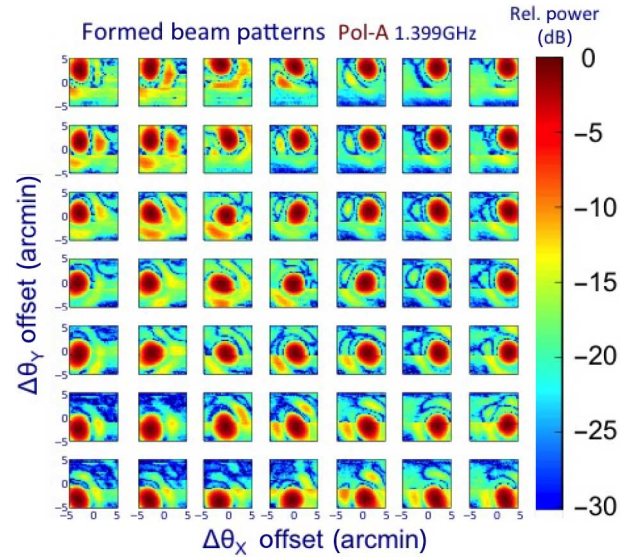

Fig. 28. Digitally formed normalized beams patterns in the sky FOV of the PAF from the calibration data.
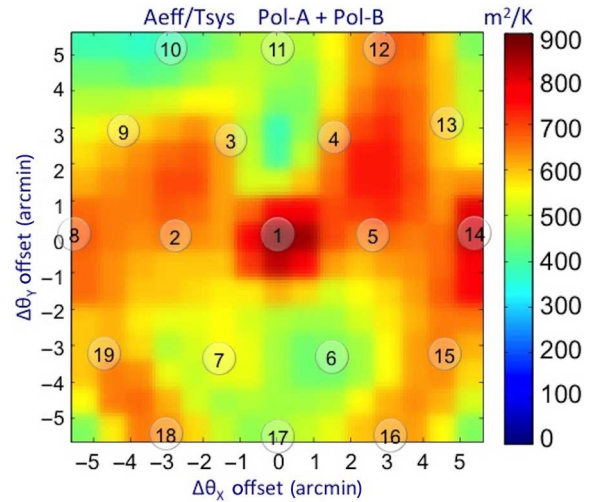
Fig. 29. Measured combined (Pol-A+Pol-B) sensitivity Map $A_{\text{eff}}/T_{\text{sys}}$ in m^2/K in sky coordinates. Note that channels 3-A, 4-B, 7-A, and 13-B were not working. Also, as mentioned earlier there is diminished sensitivity on dipoles 6, 10, and 17.

Fig. 29 includes the approximate locations of each individual dipole beam in the sky extracted from the measured individual beam patterns shown in Figs. 26 and 27. The hexagonal grid is elongated in the azimuth direction, due to the offset corrector optics of the Arecibo radio telescope. In the case of a single dipole, the peak sensitivity coincides with the direction of the dipole beam in the sky. For an array, the maximum sensitivity lies in between the individual dipole beam directions. See, e.g., the case in the direction of dipoles 2, 3, and 9, or 4, 5, and 13. The sensitivity map also reveals the effects of poor sensitivity channels (with $\sim$450m^2/K) due to nonworking channel elements: 3-A, 4-B, 7-A, 13-B, or dipoles 6, 10, and 17, which were working but with diminished sensitivity. In the case of dipole 3 and 4, in which one of the opposite polarizations in each dipole was not working (i.e., 3-A and 4-B), there is actually a minimum in the sensitivity between them.

Using an average sensitivity of $750 \, \mathrm{m^2/K}$ produced by working LNAs, and assuming 70% aperture efficiency, we obtain a beam-formed system temperature of about 36 K for the fully cryogenic PAF camera, a 16-K reduction compared with the individual channel system temperature.

V. CONCLUSION

We have developed a fully cryogenic PAF camera with 19 dual-polarized elements. Through a careful cryo and electromagnetic design, we have demonstrated the feasibility of large vacuum windows, in this case 70 cm in diameter, for large format cryo-PAF cameras. We deployed the cryo-camera on the Arecibo radio telescope for testing, and through several calibration runs, we obtained peak sensitivities as large as $850 \, \mathrm{m^2/K}$ with an average value of $750 \, \mathrm{m^2/K}$. These tests indicate that system temperatures of the order of 36 K are feasible. These are two important milestones that enable the possibility of building full-scale, large-format, cryo-PAF camera instruments for large-aperture radio telescopes.

ACKNOWLEDGMENT

REFERENCES

[1] New Worlds, "Astro 2010: The astronomy and astrophysics decadal survey," in *New Horizons in Astronomy and Astrophysics*. Washington, DC, USA: The National Academies, 2010.

[2] A. P. Chippendale and A. Schinckel, "ASKAP progress towards 36 parabolic reflectors with phased array feeds," in *Proc. URSI Gen. Assem.*, Aug. 2011, pp. 1–4.

[3] W. A. van Capellan, L. Bakker, and T. A. Osterloo, "Experimental results of the APERTIF phased array feed," in *Proc. URSI Gen. Assem.*, Aug. 2011, pp. 1–4.

[4] J. Landon *et al.*, "Phased array feed calibration, beamforming, and imaging," *Astron. J.*, vol. 139, pp. 1154–1167, 2010.

[5] G. Cortes-Medellin *et al.*, "Field of view characterization of Arecibo radio telescope with a phased array feed," in *Proc. IEEE Int. Antennas Propag. Symp. (AP-S)*, Spokane, WA, USA, Jul. 2011, pp. 847–850.

[6] G. Hampson *et al.*, "ASKAP PAF ADE advancing an L-band PAF design towards SKA," in *Proc. Int. Conf. Electromagn. Adv. Appl. (ICEAA)*, 2012, pp. 807–809.

[7] J. Cordes, "The SKA as a radio synoptic survey telescope: Widefield surveys for transients, pulsars and ETI," *Square Kilometre Array Memo Series*, Memo 97, Sep. 2007.

[8] J. D. Bunton and S. G. Hay, "Achievable field of view of chequerboard phased array feed," in *Proc. Int. Conf. Electromagn. Adv. Appl. (ICEAA)*, Sep. 20–24, 2010, pp. 728–730.

[9] G. Cortes-Medellin and D. B. Campbell, "Arecibo focal phased array: Feasibility study and instrument concept design," in *Proc. 30th URSI Gen. Assem. Sci. Symp.*, Istanbul, Turkey, Aug. 2011, pp. 1–4.

[10] K. F. Warnick *et al.*, "Towards a high sensitivity cryogenic phased array feed antenna for the Green Bank Telescope," in *Proc. URSI Gen. Assem.*, BJ.3, Aug. 2011, pp. 1–4.

[11] ROHACELL. (2014). Evonik Industries AG Performance Polymers, Darmstadt, Germany [Online]. Available: http://www.rohacell.com

[12] R. C. Johnson, *Antenna Engineering Handbook*, 3rd ed. New York, NY, USA: McGraw-Hill, 1993, pp. 18–23.

[13] CST Microwave Studio Suit, *Advanced Topics*. Darmstadt, Germany: CST-Computer Simulation Technology, 2006–2014.

[14] S. Weinreb, J. Bardin, H. Mani, and G. Jones, "Matched wideband low-noise amplifiers for radio astronomy," *Rev. Sci. Instrum.*, vol. 80, p. 044702, 2009.

[15] *PXI Express, NI PXIe-1071 User Manual*, National Instruments 210-2013 [Online]. Available: http://sine.ni.com/nips/cds/view/p/lang/en/nid/208933

[16] D. Werthimer, "The CASPER collaboration for high-performance open source digital radio astronomy instrumentation," presented at the 30th URSI Gen. Assem. Sci. Symp., Aug. 2011.

[17] B. D. Jeffs *et al.*, "Signal processing for phased array feeds in radio astronomical telescopes," *IEEE J. Sel. Topics Signal Process.*, vol. 2, no. 5, pp. 635–646, Oct. 2008.

German Cortes-Medellin (M'95) received the B.Sc. degree in physics and the B.Sc. degree in electrical engineering in 1984, the M.Sc. degree in electrical engineering in 1986, all from La Universidad de los Andes, Bogotá, Colombia, and the Ph.D. degree in electrical and computer engineering from the University of Massachusetts, Amherst, MA, USA, in 1993.

From 1994 to 1998, he was a Professor with the Department of Electrical Engineering, La Universidad de los Andes. Form 1998 to 2000, he was a Senior Microwave Engineer with Vertex RSI, Santa Clara, CA, USA, working in the optical design of large antenna reflectors including the 64-m Sardinia radio telescope, and in the design of microwave feed antenna systems. From 2000 to 2012, he was with the National Astronomy and Ionosphere Center (NAIC), Cornell University, Ithaca, NY, USA, developing instrumentation for the Arecibo radio telescope, including multi pixel feed cameras and focal phased array optical design. Since 2012, he has been with the Center for Radiophysics and Space Research (CRSR). His research interests include electromagnetic optics, ultra wide band feed antennas, radio telescope design, microwave instrumentation, computational electromagnetics, microwave, millimeter and submillimeter wave imaging.

Amit Vishwas received the B.Tech degree in information technology from the National Institute of Technology Karnataka (NITK), Surathkal, India, and the M.Eng. degree in electrical and computer engineering and the M.S. degree in astronomy from Cornell University, Ithaca, NY, USA, in 2009, 2010, and 2014, respectively. He is currently pursuing the Ph.D. degree in astronomy at Cornell University.

His research interests include spectroscopic studies of galaxies in the early universe using redshifted far-IR forbidden line emission to characterize their environment and star formation activity, TES bolometer characterization, and submillimeter instrumentation.

Stephen C. Parshley received the B.A. degree in physics from Ithaca College, Ithaca, NY, USA and the B.S. degree in mechanical engineering from Cornell University, Ithaca, NY, USA, both in 1998, and the M.Eng. degree in applied and engineering physics from Cornell University, in 2009.

He is currently working at the Center for Radiophysics and Space Research, where he designs, builds, and deploys cryogenic instruments for astronomical research.

Mr. Parshley is a Member of the American Society of Mechanical Engineers, the Cryogenic Society of America, and the Society of Photo-Optical Instrumentation Engineers.

Donald B. Campbell received the B.Sc. and M.Sc. degrees in physics from the University of Sydney, Sydney, N.S.W., Australia, in 1962 and 1964, respectively, and the Ph.D. degree in astronomy and space sciences from Cornell University, Ithaca, NY, USA, in 1971.

He is a Professor with the Department of Astronomy, Cornell University. From 1971 to 1987, he was on the Staff of the Arecibo Observatory in Puerto Rico, working on radar studies of planets and satellites with emphasis on imaging the surface of Venus beneath its dense cloud cover. He served as Associate Director and Director of the Observatory. In 1988, he joined as the Faculty with the Department of Astronomy, Cornell University continuing his planetary studies including as a Co-Investigator on the Magellan radar mission to Venus. He was involved with the 1990s upgrading of the Arecibo telescope, served as Associate Director of the National Astronomy and Ionosphere Center, which managed the Arecibo Observatory for Cornell and the National Science Foundation, from 1993 to 2004 and as its Director from 2008 to 2011.

Dr. Campbell is a Fellow of the American Association for the Advancement of Science, and a Member of the American Astronomical Society and the American Geophysical Union.

Phil Perilatt received the B.S. degree in physics from Stanford University, Stanford, CA, USA, in 1975.

He is currently a Senior Software Specialist at the National Astronomy and Ionosphere Center, Arecibo, Puerto Rico, since 1983.

Richard Black (S'13) received the B.S. degree in computer engineering and the M.S. degree in computer and electrical engineering from Brigham Young University (BYU), Provo, UT, USA, in 2012 and 2014, respectively, where he is working toward the Ph.D. degree.

His research is focused on array signal processing with an emphasis on radio astronomy applications, radio-frequency interference mitigation, and transient detection and parameter estimation using phased array feeds. He has also worked on phased array receiver systems for array signal processing algorithm development and scientific use on various radio telescope instruments including the Greenbank 100-meter telescope.

Mr. Black served four years (2011–2015) in the presidency of the BYU chapter of IEEE-Eta Kappa Nu with two years (2013–2015) as its President.

Jay Brady, photograph and biography not available at time of publication.

Karl F. Warnick (SM'04–F'13) received the B.S. degree (*magna cum laude*, with University Honors) in electrical engineering and mathematics from University Honors, OH, USA, and the Ph.D. degree in electrical engineering from Brigham Young University (BYU), Provo, UT, USA, in 1994 and 1997, respectively.

From 1998 to 2000, he was a Postdoctoral Research Associate and Visiting Assistant Professor with the Center for Computational Electromagnetics, University of Illinois at Urbana-Champaign, Champaign, IL, USA. Since 2000, he has been a Faculty Member with the Department of Electrical and Computer Engineering, BYU, where he is currently a Professor. In 2005 and 2007, he was a Visiting Professor with the Technische University, Mnchen, Germany. He has authored many scientific articles and conference papers on electromagnetic theory, numerical methods, remote sensing, antenna applications, phased arrays, biomedical devices, and inverse scattering, and is the author of the books *Problem Solving in Electromagnetics, Microwave Circuits, and Antenna Design for Communications Engineering* (Artech House, 2006), *Numerical Analysis for Electromagnetic Integral Equations* (Artech House, 2008), and *Numerical Methods for Engineering: An Introduction Using MATLAB and Computational Electromagnetics Examples* (Scitech, 2010).

Dr. Warnick has served the Antennas and Propagation Society as a Member and Co-Chair of the Education Committee and as Senior Associate Editor of the IEEE TRANSACTIONS ON ANTENNAS AND PROPAGATION AND ANTENNAS. He has been a Member of the Technical Program Committee for the International Symposium on Antennas and Propagation for several years and served as the Technical Program Co-Chair for the Symposium in 2007. He is recipient of National Science Foundation Graduate Research Fellowship, Outstanding Faculty Member Award for electrical and computer engineering, the BYU Young Scholar Award, the Ira A. Fulton College of Engineering and Technology Excellence in Scholarship Award, and the BYU Karl G. Maeser Research and Creative Arts Award.

Brian D. Jeffs (M'90–SM'02) received the B.S. (*magna cum laude*) and M.S. degrees from Brigham Young University, Provo, UT, USA, and the Ph.D. degree from the University of Southern California, Los Angeles, CA, USA, in 1978, 1982, and 1989, respectively, all in electrical engineering.

He currently holds the rank of Professor with the Department of Electrical and Computer Engineering, Brigham Young University, where he lectures in the areas of signals and systems, digital signal processing, probability theory, and stochastic processes. Previous employment includes Hughes Aircraft Company where he served as a Systems Engineer in sonar signal processing with the antisubmarine warfare group. His research interests include array signal processing for radio astronomy and radio frequency interference mitigation.

Dr. Jeffs was a Vice General Chair of IEEE ICASSP-2001 held in Salt Lake City, UT, USA. He was a Member of the Executive Organizing Committee for the 1998 and 2015 IEEE DSP Workshops, co-organized the 2010 Workshop on Phased Array Antennas Systems for Radio Astronomy, and served several years as Chair of the Utah Chapter of the IEEE Communications and Signal Processing Societies.